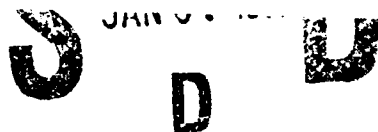


R-129
original

2

AD-A244 254



Nonlinear Influence of Mesoscale Landuse on Weather and Climate

(Submitted to *J. Climate*)

R.A. Pielke¹, G.A. Dalu^{2,3}, J.S. Snook⁴, T.J. Lee¹, and T.G.F. Kittel^{2,5}

Originally Submitted: December, 1990

~~April 24, 1991~~ May 1, 1991
(Revised)

This document has been approved
for public release and sale; its
distribution is unlimited.

¹Department of Atmospheric Science, Colorado State University, Fort Collins, Colorado 80523, USA

²Cooperative Institute for Research in the Atmosphere (CIRA), Colorado State University, Fort Collins, Colorado 80523, USA

³Institute for Atmospheric Physics (IFA-ARF-CNR), Rome, Italy

⁴Forecast Systems Laboratory, National Oceanic and Atmospheric Administration (NOAA), 325 Broadway, Boulder, Colorado 80303, USA

⁵Natural Resource Ecology Laboratory, Colorado State University, Fort Collins, Colorado 80523, USA

91-18123



Abstract

This paper demonstrates that the influence on the atmosphere of mesoscale landscape spatial variability must be parameterized (or explicitly modeled) in larger scale atmospheric model simulations including general circulation models. The mesoscale fluxes of heat which result from this variability are shown to be of the same order of magnitude and with a different vertical structure than found for the turbulent fluxes. These conclusions are based on experiments in which no phase changes of water were permitted. When, for example, cumulus clouds organized in response to the landscape pattern develop, the mesoscale influence on larger scale climate is likely to be even more important.

To parameterize surface thermal inhomogeneities, the influence of landscape must be evaluated using spectral analysis or an equivalent procedure. For horizontal scales much less than the local Rossby radius, based on the results of Dalu and Pielke (1991) the surface heat fluxes over the different land surfaces can be proportionately summed and an average grid-area value used as proposed in Avissar and Pielke (1989). Moisture fluxes can probably be represented in the same fashion as for heat fluxes. For larger scale spatial variability, however, the mesoscale fluxes must also be included as shown in this paper. While the linear effect could be parameterized using a procedure such as presented in Dalu and Pielke (1991), where the spectral analysis is used to fractionally weight the contributions of the different spatial scales, the complete vertical mesoscale heat flux requires the incorporation of nonlinear advective effects. To include the nonlinear contribution of each scale, numerical model simulations for the range of observed surface and overlying atmospheric conditions must be performed.

1. Introduction

This paper illustrates, using examples, the observed spatial variability of landscape and demonstrates how this variability affects the lower tropospheric fluxes of energy in the absence of clouds. This variability is associated with (i) man-caused changes; and (ii) natural variations in vegetation and soil composition. Short term weather effects (e.g. rainfall history) as well as local micro-environmental conditions (e.g. soil structure) influence the natural variations.

Using nonlinear model results, the modification of the overlying atmosphere due to spatial variability of landscape is evaluated. The emphasis of the paper will be on the influence of variable heat flux which results from the landscape pattern on flat terrain. Subsequent papers will explore the effect of landscape variability in irregular terrain.

Modifications of atmospheric conditions due to landscape variability, as contrasted with a uniform landscape, occur due to (i) changes in the surface layer fluxes, and (ii) resultant coherent wind circulations which develop as a result of the spatial variability in these heat fluxes. In this paper, we will concentrate on the influence of heat fluxes. If the spatial scale of forcing is small enough (e.g., much smaller than the depth of the boundary layer), it should be sufficient to spatially average the different surface layer fluxes (proportionally weighted by the fractional coverage of a grid area by different land surface types) as discussed in Avissar and Pielke (1989). For larger scales, however, the influence of mesoscale fluxes of heat must also be considered since they can be on the same order as and have a different vertical distribution than the turbulent fluxes.

Changes in average and spatial variations in landscape are important in influencing atmospheric conditions. Using a simple energy balance analysis, for example, Pielke and Avissar (1990) have shown that for small changes in average local surface characteristics

$$\Delta T_E = -3.04 \times 10^9 \frac{\Delta A}{T_E^3}.$$

T_E is an equilibrium temperature in units of degrees Kelvin and A is the albedo. A value of the solar insolation at the surface of 690 W m^{-2} is used in the equation. Thus locally, if an energy

balance equilibrium were achieved, a change of albedo of +1% would result in a decrease of T_E of about 1.4°C.

André et al. (1990) suggest that there are two types of non-homogeneous landscapes:

“(i) the ‘disorganized’ land surfaces, for which the characteristic horizontal scale is smaller than about 10 km, so that no apparent coherent response can be traced in the atmosphere since the boundary-layer turbulence averages everything out;

(ii) the ‘organized’ land surfaces, for which the characteristic length is greater than 10 km, so that the atmosphere develops a coherent response at the mesoscale.”

As indicated in their paper, however, much work yet remains to devise procedures to accurately estimate surface fluxes where there is significant surface inhomogeneity. Our paper further examines the categorization (i) and (ii) postulated in their paper.

2. Observational Evidence

Pielke and Kennedy (1980), Young and Pielke (1983), Young et al. (1984), and Steyn and Ayotte (1985) used spectral analysis to document spatial variability of terrain. As discussed in those papers, such an analysis is essential in order to determine the minimum horizontal grid interval which is required in order to explicitly resolve the terrain forcing. Alternatively, a parameterization of the smaller scale terrain influence on the overlying atmosphere could be developed for use in a coarser grid model.

We propose that a similar spectral analysis should be completed for landscape variability. In areas with both variable terrain and landscape variations, cross spectra and quadrature analysis should be completed in order to ascertain the correlation of landscape and terrain as a function of spatial scale, aspect, etc.

Vegetation biomass and leaf area index (LAI) are constraints over terrestrial surface fluxes of energy, moisture, and momentum that vary spatially from micro- (<100 m), landscape (100 m - 10 km), regional (10 - 1000 km) to global scales. Variability at landscape and greater scales is observable using satellite-based data at appropriate resolutions [e.g., 20 m (Satellite Probatoire d'Observation de la Terra - SPOT), 1.1 km and 4.4 km modes of the NOAA-polar orbiter Advanced Very High Resolution Radiometer (AVHRR)]. Spectral vegetation indices based on these data have been used to assess spatial patterns in vegetation condition in terms of above ground green biomass (e.g., Davis et al., 1990, 1991), LAI (e.g., Running et al., 1989), and crop yield (e.g., Barnett and Thompson, 1983). Annual or growing season integrals of Normalized Difference Vegetation Index (NDVI) and other indices have been related to annual net primary production (Goward et al., 1986). These indices are also useful in following seasonal and interannual dynamics of vegetation across broad regions (Tucker et al., 1985, 1986; Justice et al., 1985). The success of vegetation indices to illustrate spatial and temporal variability in above ground vegetation arises from their relationship to intercepted photosynthetically active radiation, canopy photosynthetic capacity, and maximum canopy conductance (Sellers, 1985). Since maximum canopy conductance constrains surface H₂O and CO₂ fluxes, NDVI may prove valuable as a forcing variable in biosphere-atmosphere exchange models linked to atmospheric circulation models (Schimel et al., 1991).

At the landscape scale, field and SPOT satellite data collected during FIFE (First ISLSCP Field Experiment; ISLSCP is the International Satellite Land Surface Climatology Project) in a tall grass prairie region in eastern Kansas show that biomass and LAI vary up to five-fold with topographic position (across 200 m wide, 30 m deep watersheds) and as a function of grazing and burning management within the 15 km x 15 km FIFE site (Schimel et al., 1991; Kittel et al., 1990; Davis et al., 1990). Such variation in surface biological properties (biomass, LAI) reflects the impact of topography and land use on water and nutrient availability (Schimel et al., 1991). Integrated across the landscape, variation in topography and vegetation appears to influence the

Statement A per telecon
Dr. Robert Abbey ONR/Code 1122
Arlington, VA 22217-5000

NWW 1/6/92

Availability Codes	
Dist	Avail. Codes
A-1	

development and structure of the planetary boundary layer as observed by LIDAR (Schols and Eloranta, 1991) and aircraft (Desjardins et al., 1990).

At the regional scale, AVHRR NDVI data for the central and northern U.S. Great Plains in early May 1990 (Figure 1) show fine grain spatial variation at the data set's 1 km resolution. While local topography, soils, and land use vary at such fine scales, soil, climate, and drainage patterns also vary at the regional scale influencing patterns in land use and vegetation (Parton et al., 1987; Burke et al., 1989, 1990, 1991). This is reflected in 50–200 km-scale variation in NDVI across the Great Plains (Figure 1). Large areas with minimum NDVI include rangelands in southeastern Colorado (influenced by a regional minimum in annual precipitation) and the Sand Hills in western and central Nebraska (edaphic-influenced). Maxima occur over the rain-fed winter wheat and grain sorghum region of east central Kansas (bounded on the east by the Flint Hills with lower spring NDVI) and irrigated croplands adjacent to major rivers such as the South Platte in northeastern Colorado. Such contrasts in NDVI reflect contrasts in land use and vegetation at scales that are important in forcing mesoscale circulations (Segal et al., 1988). On a somewhat larger spatial scale, Lanicci et al. (1987) concluded that the spatial distribution of soil moisture over the southern Great Plains and the Mexican Plateau significantly influence the evolution of convective rainfall patterns over Texas and Oklahoma.

Spatial contrasts at the regional scale can shift during the course of a year because vegetation under different land management (e.g., irrigated cropland vs. native rangeland) have different seasonal patterns of growth and senescence (or harvest). The sharp gradient in spring 1990 NDVI between central Kansas (cropland) and the Flint Hills (rangeland) (Figures 1 and 2a) is reversed by mid-summer (Figure 2b) due to the harvest of winter wheat and rangeland greenup. At the scale of a week, contrasts in plant condition can develop in dry land areas reflecting rainfall patterns from storms. Interannual variability in climate also results in significant year-to-year differences in regional patterns in vegetation biomass as suggested by NDVI observations, and ecosystem simulation modeling of the 1988 drought over Kansas (Burke et al., 1991).

3. Nonlinear Analysis of the Influence of Landscape Variability

Since no general analytic theory exists to determine the influence of nonlinear effects on the results of Dalu and Pielke (1991) in which a linear model was applied to evaluate the importance of spatially varying heat fluxes, we must utilize numerical model results to evaluate the relative contribution of turbulent and mesoscale heat effects as a function of the spatial scales of the surface forcing. Moreover, while linear results provide concise general analytic expressions which could be used as part of a parameterization scheme for use in a coarse grid model, the range of possible landscapes and overlying atmospheric conditions must be integrated using the numerical model in order to develop a general quantitative parameterization. The linear results reported in Dalu and Pielke (1991), however, did document that mesoscale circulations are likely to be important mechanisms of vertical heat transport when the size of the surface thermal forcing is on the scale of the local Rossby radius. For heat patches much less than this scale, the surface heat fluxes can be spatially averaged, as suggested in Avissar and Pielke (1989). The large eddy simulation study reported in Hadfield et al. (1991a, b), where the influence of small scale heat patches (of widths of 1.5 km and 4.5 km) on convective boundary layer structure were investigated, support this conclusion.

In this section, several generic nonlinear numerical simulations are performed to demonstrate the procedure to develop a general parameterization, as well as to further document the importance of mesoscale heat fluxes as contrasted with turbulent heat fluxes. In addition, a specific example of a landscape contrast and its influence on turbulent and sensible heat fluxes is presented.

a. Influence of spatial landscape variability on vertical heat flux in the absence of a larger scale wind flow

1) Homogeneous vs. nonhomogeneous surfaces

A comparison of the domain average vertical heat flux for homogeneous and nonhomogeneous surfaces shows the importance of spatial landscape variability. The domain average vertical heat

flux for the homogeneous surface case is equal to the grid averaged subgrid scale correlation, $\overline{w''\theta''}$, which is parameterized by $-K_\theta \frac{\partial \bar{\theta}}{\partial z}$ where K_θ is the vertical exchange coefficient estimated from a Smagorinsky type eddy viscosity with a Richardson number dependence. For the nonhomogeneous case, the explicit heat flux due to mesoscale circulations induced by the variable landscape needs to be considered in addition to the subgrid scale flux. Thus, the domain average total vertical heat flux is represented by

$$\langle w'\theta' \rangle_D + \langle \overline{w''\theta''} \rangle_D$$

where $w'\theta'$ is the resolvable mesoscale circulation and $\overline{w''\theta''}$ is the subgrid scale contribution. The domain average operation for the simulations with the periodic domains which are discussed in this section (i.e., cyclic lateral boundary conditions are used) is defined as

$$\langle A \rangle_D = \frac{1}{N_x} \sum_{i=1}^{N_x} A_i$$

where A is any quantity, the subscript D indicates the domain average and the variable N_x is the total horizontal grid points in that domain. The two components of heat fluxes are defined as¹:

- resolvable heat flux

$$\langle w'\theta' \rangle_D = \langle (w - \langle w \rangle_D)(\theta - \langle \theta \rangle_D) \rangle_D$$

- subgrid scale heat flux

$$\langle \overline{w''\theta''} \rangle_D = -\langle K_\theta \frac{\partial \bar{\theta}}{\partial z} \rangle_D.$$

¹ Note that with cyclic boundary conditions, $\langle w \rangle_D = 0$. Thus, $\langle w'\theta' \rangle_D = \langle w\theta - \langle w \rangle_D \theta - w \langle \theta \rangle_D + \langle w \rangle_D \langle \theta \rangle_D \rangle_D = \langle w\theta - w \langle \theta \rangle_D \rangle_D$. Since $\langle w \langle \theta \rangle_D \rangle_D = \left(\int_D w \langle \theta \rangle_D dx \right) / D = \langle \theta \rangle_D \left(\int_D w dx \right) / D = \langle \theta \rangle_D \langle w \rangle_D = 0$, $\langle w'\theta' \rangle_D = \langle w\theta \rangle_D$. This was also verified in the model computations.

2) Model characteristics

Two dimensional model simulations were run using the Colorado State University (CSU) Regional Atmospheric Modeling System (RAMS) in its nonhydrostatic, anelastic form and applying cyclic lateral boundary conditions (Tremback *et al.*, 1986, Schmidt and Cotton, 1990). A surface energy budget (Tremback and Kessler, 1985) was used to diagnose the surface temperature variation during the day. The horizontal grid interval was 1 km and the vertical grid was stretched by a factor of 1.1 with the lowest layer set to 150 m. The homogeneous case was initialized at 0600 Local Standard Time (LST) with a uniform land surface at 30° latitude for 21 June, an initial surface temperature of 293 K, and no horizontal wind. A minimum value of shearing stress (i.e., $u_* > 0.01 \text{ m s}^{-1}$) was specified, however, in order to generate surface heat fluxes. Six nonhomogeneous surface cases were initialized with alternating land and water strips equal in width to 4, 8, 16, 32, 64, and 96 km, respectively. N_x was 16 for the 4 km case, 32 for the 8 km case, 64 for the third and fourth nonhomogeneous cases, 128 for the 64 km case, and 192 for the last case. Thus, in the 4, 8, and 16 km strips experiment, there were 2 sets of alternating surfaces, while only one set was used for the larger strips. All simulations were run to 12 h.

3) Model results

Model results are shown for the seven cases at model levels 2 through 9. The model levels correspond to the heights: level 1 = 0 m; level 2 = 150 m; level 3 = 315 m; level 4 = 497 m; level 5 = 696 m; level 6 = 916 m; level 7 = 1157 m; level 8 = 1423 m; and level 9 = 1715 m. Figure 3 shows time cross sections of the domain average total vertical heat flux. For the homogeneous case, the total vertical heat flux is equal to the subgrid scale heat flux since the explicit mesoscale contribution is zero. The total vertical heat flux reaches a maximum at 6 h coincident with the time of maximum heating. The 6 h magnitudes decrease with height and range from zero at levels 1157 m and above (which is above the planetary boundary layer) to 475 W m^{-2} at 150 m and 315 m.

Total vertical heat flux profiles are similar for the cases with land mass widths of 64 km and greater (Figs. 3f,g). Total heat flux rises with time at a near uniform rate before leveling off at a magnitude of 350 W m^{-2} at 150 m. The peak heat flux is reached later in the day for larger land mass widths. Following this time, the total heat flux reduces to near zero by 12 h. The total heat flux for the 64 and 96 km cases is less than the homogeneous total heat flux for the first 6 h. After 6 h, the 150 m heat fluxes are comparable but the heat flux at the higher levels from 315 m to 1157 m are significantly greater for the nonhomogeneous cases. A negative mesoscale heat flux is observed for levels just above the top of the boundary layer. This is observed at 6 h at 1157 m and 1423 m and at 8 h at the 1715 m level. The mesoscale heat fluxes at 1157 m and 1423 m become positive for the later time periods when the levels are part of the boundary layer.

Similar profiles of total vertical heat flux are observed for the smaller land mass width cases of 4, 8 and 16 km (Figs. 3b-d). The 150 m total heat flux reaches a maximum of $300\text{-}375 \text{ W m}^{-2}$ at 6 h and remains high for a couple of hours before falling off. Total heat flux values at the higher levels within the boundary layer rise with some fluctuations and peak at 7 to 9 h. As with the larger width cases, the nonhomogeneous total heat flux is less than the homogeneous total heat flux during the first 6 h, comparable at 150 m after 6 h, and significantly greater for the higher levels after 6 h. The negative mesoscale heat fluxes observed at 1157 m, 1423 m, and 1715 m occur when these levels are just above the top of the boundary layer.

The 32 km width land mass case is a hybrid of the two scenarios described above (Fig. 3e). The total heat flux rises uniformly for the first 6 h similar to the larger width cases. After the heat flux peaks at 6 h, it decreases slowly for several hours before dropping off more rapidly similar to the smaller width cases. Comparing the homogeneous and 32 km nonhomogeneous cases, the total heat fluxes show similar results as noted above.

Dividing the total vertical heat flux into subgrid scale heat flux and explicit vertical heat flux due to mesoscale circulations provides more insight into the above results. Consistent with the linear results (Dalu and Pielke, 1991), the mesoscale heat flux contribution is positive within the

planetary boundary layer (PBL) over land and negative above. This result is enhanced in the numerical model results due to the horizontal wind convergence into the upward motion regions. The resultant asymmetry from this nonlinear advection results in a positive skewness of the vertical velocity in the PBL. The upward transfer of the superadiabatically stratified atmosphere near the surface, which, much like large eddies in the boundary layer, results in an upward heat flux. Figure 4 shows several cross sections of the domain average subgrid scale vertical heat flux and the domain average mesoscale vertical heat flux at 150 m, 315 m, and 497 m for the six nonhomogeneous cases.

For the nonhomogeneous cases, solar heating of the land masses creates a sea breeze. A sea breeze front forms on each side of the land mass and propagates inland with time. Eventually, the two sea breeze fronts collide resulting in a single, strong upward vertical velocity branch over the center of the land mass. The collision occurs later in the day for the larger land masses (e.g., see also Xian and Pielke, 1991). Following the collision, two vertical circulation cells are maintained for the remainder of the day with the single upward branch centered over the land mass.

Results for the cases with land mass widths of 32 km and greater are shown in Figs. 4d,e,f. Prior to the sea breeze collision, the subgrid scale heat flux exceeds the mesoscale induced heat flux. The difference is greater for the larger land masses where the boundary layer is heated for a longer time period providing stronger subgrid scale heat fluxes. As the sea breeze fronts near collision, the upward vertical velocity becomes much stronger and the mesoscale heat flux exceeds the subgrid scale heat flux. The mesoscale heat flux reaches a maximum of between 200 and 300 W m^{-2} for all three cases (32, 64, and 96 km) at the time of sea breeze collision. At this time, the mesoscale heat flux exceeds the subgrid scale heat flux by 33% (96 km) and 150% (32 km) at 150 m and is even more important at 315 m and 497 m. Following the sea breeze collision, the strength of the upward branch decreases with time and the mesoscale heat flux also decreases. Reduced heating of the boundary layer behind the sea breeze front causes the subgrid scale heat flux to decrease with time as well. Thus the mesoscale heat flux remains greater than the subgrid scale heat flux for

the remainder of the day. The significant mesoscale heat flux after 6 h allows the nonhomogeneous total heat flux to be greater than the homogeneous total heat flux.

Different results are observed for the 4, 8, and 16 km cases (Figs. 4a,b,c). Since the sea breeze collision occurs earlier in the day, the boundary layer does not have much time to heat and hence the subgrid scale heat flux is smaller. The upward vertical velocity increases more rapidly than for the larger land masses and the mesoscale heat flux exceeds the subgrid scale heat flux from the start. Although the sea breeze collision occurs near 2 h (0800 LST) for the 8 km case, the mesoscale heat flux continues to rise significantly with time. Two factors appear to play a role in this result. First, continued heating in the morning hours allows the vertical velocity branch to continue increasing in magnitude following sea breeze collision. Second, the downward branches are consolidated into smaller horizontal regions. Hence, stronger downward branches are observed in the cooler post-frontal air which provides a positive contribution to the mesoscale heat flux. For the 16 km case, the sea breeze collision occurs near 5 h and the mesoscale heat flux reaches a maximum. However, the mesoscale heat flux maintains its magnitude after 5 h due to the same mechanisms described above.

A secondary pulse is also observed in the mesoscale heat flux for the 8 and 16 km cases. The stronger, consolidated downward branches reinforce the sea breeze circulation and cause a second surge to move inland. When these collide, the upward vertical motion increases temporarily which creates the secondary pulse in the mesoscale heat flux. The mesoscale heat flux remains dominant over the subgrid scale heat flux for the remainder of the day. Since the mesoscale heat flux remains significant during the afternoon, the nonhomogeneous total vertical heat flux is greater than the homogeneous heat flux after 6 h.

4) Summary

Mesoscale circulations induced by spatial landscape variability make an important contribution to the domain average total vertical heat flux in the absence of a larger scale wind flow. For

landscape variability with a larger horizontal scale, the subgrid scale heat flux is larger than the mesoscale heat flux for the early part of the day. As the mesoscale circulations evolve, the mesoscale heat flux becomes dominant by afternoon and remains dominant for the remainder of the day. For smaller horizontal scales, the mesoscale circulations evolve more rapidly and the mesoscale heat flux becomes dominant soon after the commencement of solar heating and remains dominant for the remainder of the day. Differences exist between the total heat fluxes of a homogeneous surface and the nonhomogeneous surfaces. Initially, the total heat flux is greater for the homogeneous case. However, after maximum solar heating occurs, explicit vertical heat flux due to mesoscale circulations continues to be significant and allows the nonhomogeneous total vertical heat flux to significantly exceed the homogeneous total vertical heat flux. The mesoscale heat flux is a significant contributor to the domain average total heat flux for all cases and should not be ignored in coarse resolution models which do not resolve these mesoscale circulations.

b. Influence of spatial landscape variability on vertical heat flux in the presence of larger scale wind flow

1) Model experiments

A total of 12 model simulations were conducted to investigate the effects of a large scale wind on the vertical heat flux over a variable landscape. Separate experiments with uniform horizontal winds of 5, 10, and 15 m s⁻¹ were performed using 4, 8, 16, and 32 km strips. Except for the large scale wind flow, the experiments are identical to the uniform strip cases performed in Section 3a.

2) Model results

The domain average total vertical heat fluxes show similar characteristics for the various landscape cases with wind. Figure 5 shows cross sections of the total vertical heat flux at model levels corresponding to 150 m through 1715 m (levels 2-9) for the three wind experiments with 8 km strips. The total heat fluxes are reduced with increasing wind speed and greater reductions are

noted for smaller strip widths (e.g., see Figure 7a). For example, a comparison of the calm and 5 m s^{-1} initialized wind simulations at 150 m shows no significant total heat flux reduction for the 32 km strip case while a 150 W m^{-2} drop is noted for the 4 km strip case. The effects of wind on the total heat flux are less pronounced with larger width strips. Maximum total heat fluxes are attained near 8 h for all the wind cases which is about 2 h later than for the calm cases.

The horizontal wind prevents a tight horizontal temperature gradient to develop in the atmosphere along both coasts and is responsible for the decreased total vertical heat flux (i.e., due to a weaker horizontal pressure gradient force). In contrast, with calm large scale flow, strong horizontal pressure gradients can develop along both coasts. The effects of mixing are better understood by dividing the total vertical heat flux into subgrid scale vertical heat flux and explicit vertical heat flux due to mesoscale circulations. Again, results are similar for the various landscape cases with wind. Figure 6 shows time cross sections of the domain average subgrid scale heat flux and the domain average mesoscale vertical heat flux at 150 m, 315 m, and 497 m for the three wind experiments using 8 km strips. Except for the 5 m s^{-1} wind speed cases using 16 and 32 km strips, the subgrid scale heat flux profiles are nearly identical regardless of strip width and wind speed. A well defined peak of subgrid scale heat flux is reached at 7 h with a value of about 230 W m^{-2} at 150 m, which is significantly greater than the subgrid scale heat flux for the calm case. Mixing by the wind allows for stronger subgrid scale heat fluxes. The effect is especially pronounced over water where the calm case has no subgrid scale vertical heat flux while the flux is significant for the wind cases. The effects of mixing are reduced for the lower wind speed, larger width strip cases (i.e., 5 m s^{-1} wind speed with 16 and 32 km strips). The subgrid scale heat flux peaks at 6 h with a lower value of about 175 W m^{-2} ; hence, falling between the calm experiments and the other wind cases.

Mesoscale heat fluxes, in contrast to the subgrid scale fluxes, decrease with greater horizontal wind speeds and are significantly less than the mesoscale flux for the calm case. The horizontal temperature gradients are less pronounced which leads to a smaller domain averaged mesoscale

heat flux. For the wind cases, the mesoscale heat flux reaches a maximum later in the day between 8 and 10 h. During the later time periods, the mesoscale heat flux exceeds the subgrid scale heat flux at 315 m and 497 m, but only exceeds the subgrid scale heat flux at 150 m for the 5 m s^{-1} cases with 16 and 32 km strips.

3) Summary

When a prevailing wind occurs, the more diffuse horizontal temperature gradient inland from at least one of the coastlines reduces the domain average mesoscale vertical heat flux with the effect more pronounced with smaller width strips. Over variable landscape, the domain average subgrid scale vertical heat fluxes increase while the domain average mesoscale vertical heat fluxes decrease compared to the respective fluxes for the calm cases. For all situations, except the light wind speed and large width strip cases (i.e., 5 m s^{-1} wind speed over 16 and 32 km strips), the large decrease in the mesoscale heat flux overcomes the significant increase in the subgrid scale heat flux accounting for a smaller total domain average heat flux in the wind experiments. Although the mesoscale heat flux is smaller, it still makes a significant contribution to the total heat flux at the later time periods.

c. Influence of spatial landscape variability on time averaged vertical heat flux

A comparison of the 12 h vertically integrated, time and domain averaged vertical heat flux for the 19 model experiments (one homogeneous with no large scale flow, six nonhomogeneous with no large scale flow and 12 nonhomogeneous with large scale flow) is shown in Figure 7. The total vertical heat flux for the homogeneous case is larger than the other experiments except the 96 km, no initial wind case. Note that the homogeneous experiment has double the land surface compared to the other simulations. Thus, neglecting the nonlinear effects due to mesoscale circulations, one would expect the total heat flux for the nonhomogeneous, no initial wind cases to be only half of the total flux for the homogeneous experiment. It appears that the nonhomogeneous landscape is

more efficient at putting energy from solar insolation into the atmosphere while over the domain more insolation is absorbed into the surface for the homogeneous case. This is verified through the model soil temperatures which are warmer at 12 h for the homogeneous cases than for the nonhomogeneous simulations.

The linear results suggest that as the surface strips decrease in width, the nonhomogeneous vertical heat fluxes should approach to one half of the vertical heat fluxes of the homogeneous case. The model results presented here do not corroborate this linear result. The model horizontal grid spacing is 1 km for all cases which determines the smallest resolvable strip width to be 4 km. A smaller horizontal grid spacing would be required to simulate smaller strip width cases. However, a smaller grid spacing can support a stronger horizontal pressure gradient which could lead to stronger mesoscale circulations and a misleading comparison to the larger strip width cases. The model horizontal grid spacing must always be less than or equal to 25% of the strip width (e.g., see Pielke, 1984, pg. 331) so that mesoscale circulations will always be resolvable. However, the mesoscale circulations should be confined to a shallower layer as the strip width decreases. This is only marginally observed at 497 m and above for the calm cases, but is more noticeable for the wind cases where the wind reduces the horizontal pressure gradient force.

Dividing the time averaged total vertical heat flux into subgrid scale vertical heat flux and explicit vertical heat flux due to mesoscale circulations shows some interesting differences. Only the subgrid scale vertical heat flux contributes to the total for the homogeneous case. For the non-homogeneous, non-wind experiments, the subgrid scale flux increases with increasing strip width. With increasing strip width, the mesoscale heat flux decreases for level 2 (150 m), remains about the same at 315 m and 497 m and increases slowly for the higher levels. The net result is an initial decrease in total heat flux followed by a slow increase with increasing strip size which eventually exceeds the homogeneous case for the 96 km strips despite half the surface land mass.

Two competing effects are occurring in the nonhomogeneous cases. First, the wind flow from the unheated to heated surface region creates a less unstable boundary layer which creates a smaller

subgrid scale heat flux. Second, the induced mesoscale circulations create an explicit mesoscale heat flux which more than compensates for the reduced subgrid scale heat flux leading to the higher total heat fluxes for the nonhomogeneous cases. For the smaller width strip cases, the earlier convergence of the opposing flows from the two sides of the heated surface forces the boundary layer to remain shallow and less unstable causing the subgrid scale contribution to be small. In addition, the stronger vertical circulations are maintained through the day forcing a larger mesoscale contribution. When the wind convergence occurs later in the day for the larger strip width cases the boundary layer becomes deeper and more unstable allowing a larger subgrid scale contribution. Meanwhile, the stronger and deeper vertical circulations which occur later in the day permit a significant mesoscale contribution which explain the large total heat flux for the 96 km experiment. The mesoscale contributions are significant in all cases.

For the experiments initialized with a large scale wind, the subgrid scale heat fluxes remain nearly constant for all cases and they are larger than the corresponding fluxes for the no wind situations. This is due to the wind creating a more diffuse horizontal pressure gradient force. The two exceptions are the 8 and 16 km strip cases with a 5 m s^{-1} wind where the wind effects are reduced, hence lowering the subgrid scale heat flux. The decreased pressure gradient force inland from one of the coastlines causes a significant decrease in the mesoscale contributions. The mesoscale heat flux rises slowly with increasing strip width. Again, the two exceptions are the 8 and 16 km strip cases with a 5 m s^{-1} wind where the mesoscale flux is larger due to the reduced effects of the wind on the subgrid scale fluxes. The net effect is lower total vertical heat flux compared to the non-wind cases with the total heat flux decreasing slowly with increasing wind speed and increasing slowly with increasing strip width. The mesoscale heat flux still makes a significant contribution towards the total heat flux in all cases.

The vertically integrated, time and domain averaged total vertical heat flux is relatively constant compared to the large variations in the subgrid scale and mesoscale heat fluxes. For all the nonhomogeneous simulations, these space- and time-averaged subgrid scale and mesoscale heat

fluxes are inversely correlated. Although the mesoscale contribution is significant in each of the nonhomogeneous cases, the significance to the total heat flux is reduced due to this inverse correlation. The distribution of heat with height, however, is clearly different when mesoscale circulations occur since heat can be transported to levels deeper than occurs due to subgrid heat flux alone.

d. Two-dimensional simulation of domain, resolvable, and subgrid-scale fluxes on the mesoscale when a vegetation contrast exists

1) Numerical simulation

In this section we present an example to demonstrate the non-linear effect when a realistic surface inhomogeneity exists. We have chosen our model domain to be comparable to two grid volumes of a general circulation model (GCM). However, we divided our domain into two sub-domains according to vegetation covers. Thus, we can calculate the difference in turbulent fluxes between the entire domain averaged value and the average in the sub-domains. The CSU RAMS was also used in simulations presented in this section. The parameterization of vegetation was given in Avissar and Mahrer (1988). A two-dimensional version of the model was set up over a mesoscale domain of 200 km horizontally and a top at 4 km. The number of grid points were 40×25 . Two different vegetation cover types were specified (each one covers half of the domain). The horizontal resolution was 5 km and the vertical resolution was 100 m near the ground and stretched up to 500 m resolution with a stretch ratio of 1.1. The left hand side of the domain was covered by trees ($LAI = 5.8$) with an aerodynamic roughness length of $z_0 = 2$ m and an albedo at noon of 0.15 and the right hand side was covered by irrigated wheat cropland ($LAI = 4.7$) with $z_0 = 2$ cm and an albedo at noon of 0.25. The relative stomatal resistance is a function of environmental variables as described in Avissar and Mahrer (1988). The model was started at 0600 LST and integrated for 12 hours. The initial wind was calm. The surface energy budget was driven by midsummer (1 July) solar radiation at 40° N. The underlying soil layer was 60% saturated in the root zone and was reduced linearly to the wilting point at 3 meters. This soil moisture content was large enough

in the root zone so that plants were basically evaporating near the potential rate. The difference in the evaporating rate over the two areas comes from the albedo, aerodynamic roughness, and the LAI.

A thermally direct circulation was simulated later in the afternoon due to the thermal contrast between the two different vegetation covered areas (Fig. 8). A cooler atmospheric boundary layer is found above the trees where the evapotranspiration is abundant. On the other hand, the atmospheric boundary is warmer and deeper over the crop where the evapotranspiration is relatively smaller and the vegetation heat capacity is less. Figure 8 shows the potential temperature field at the end of 12 hours. The temperature contrast in the mixed layer is as high as 4°C. Also, notice that the mixed layer is unstably stratified over the crop while it has become stably stratified over the forest. Figures 9 and 10 illustrate the horizontal and vertical wind components. The horizontal wind field near the surface is generally from the forest to the crop area with a return flow aloft. Ascending motion is found near the "front" over the crop area where a strong near surface convergence in the horizontal wind is simulated. Descending motion is observed over the forest where near surface divergence of the horizontal wind occurs.

2) Calculation of fluxes

The heat fluxes were calculated at the end of the simulation. A thermally direct circulation is found at this time so that a upward heat flux is expected in the boundary layer on the resolvable scale. The subgrid scale heat flux is also upward since the boundary layer is still convective at this time. The resolvable and subgrid scale heat fluxes are defined in Section 3 and three different domains are used in this study: (i) for the whole domain, subscript D is dropped; (ii) averaged over the forest sub-domain, $D = f$; and (iii) the crop sub-domain, $D = c$.

Figure 11 shows the resolvable and subgrid scale heat fluxes. Due to the asymmetric structure of the vertical velocity field (i.e., Figure 10) positive vertical velocity only exists above the crop and w' is greater than zero up to 1.5 km. Extending above the PBL $\langle w'\theta' \rangle_c$ becomes negative because

of the region with θ' less than zero above the PBL. We expect $\langle w'\theta' \rangle_c$ to be positive near the surface and become negative aloft. This is indeed simulated. Over the forest, the only significant feature is the negative heat flux near and above the top of the PBL which is attributed to the negative vertical velocity and cooler temperatures due to the transpiration from the trees. The total domain averaged heat flux shows positive values near the ground and negative values near and above the top of the boundary layer as expected for a thermally direct circulation. The subgrid scale heat flux over the crop shows a nearly linear profile over the crop which indicates that the boundary layer is convective. Over the forest, the subgrid heat flux is actually negative due to the stable stratification near the surface. The domain averaged subgrid heat flux profile again falls between that of the cropland and the forest.

Figure 12 shows the difference between the domain averaged heat flux and the sum of the two sub-domain averaged heat fluxes. Since there is no averaging involved in calculating the subgrid scale heat flux, the difference is zero. However, variables $\langle w \rangle_D$ and $\langle \theta \rangle_D$, which are used in calculating w' and θ' , varies with respect to the three different domains, we observe that

$$\langle w' \rangle \neq (\langle w' \rangle_t + \langle w' \rangle_c) / 2,$$

$$\langle \theta' \rangle \neq (\langle \theta' \rangle_t + \langle \theta' \rangle_c) / 2$$

thus a difference is expected when calculating the domain averaged resolvable heat flux.

3) Summary

Two primary conclusions can be extracted from this section. (1) The domain averaged subgrid scale flux is not sensitive to the averaging process, and (2) the domain averaged resolvable scale flux is highly sensitive to the averaging process because of the asymmetry in the thermally-forced mesoscale circulation.

4. Conclusions

This paper demonstrates that the influence on the atmosphere of mesoscale landscape spatial variability must be parameterized (or explicitly modeled) in larger scale atmospheric model simulations including general circulation models. Even if these larger scale models had sufficient spatial resolution they must include a diurnal cycle to represent this effect. The mesoscale fluxes of heat which result from this variability are shown to be of the same order of magnitude and with a different vertical structure than found for the turbulent fluxes. These conclusions are based on experiments in which no phase changes of water were permitted. When, for example, cumulus clouds organized in response to the landscape pattern develop, the mesoscale influence on larger scale climate is likely to be even more important.

To parameterize surface thermal inhomogeneities, the influence of landscape must be evaluated using spectral analysis or an equivalent procedure. For horizontal scales much less than the local Rossby radius, based on the results of Dalu and Pielke (1991) the surface heat fluxes over the different land surfaces can be proportionately summed and an average grid-area value used as proposed in Avissar and Pielke (1989). Moisture fluxes can probably be represented in the same fashion as for heat fluxes. For larger scale spatial variability, however, the mesoscale fluxes must also be included as shown in this paper. While the linear effect could be parameterized using a procedure such as presented in Dalu and Pielke (1991), where the spectral analysis is used to fractionally weight the contributions of the different spatial scales, the complete vertical mesoscale heat flux requires the incorporation of nonlinear advective effects. To include the nonlinear contribution of each scale, numerical model simulations for the range of observed surface and overlying atmospheric conditions must be performed.

5. Acknowledgements

We acknowledge the support of the National Science Foundation (NSF) under Grant #ATM-8915265 and Office of Naval Research under Contract #N00014-88-K-0029. G.A. Dalu acknowl-

edges the support of the Italian *ENEL-Program*. T.G.F. Kittel was supported by grants from NASA FIFE (NAG-5-910) and NSF Long-Term Ecological Research Program (BSR-88-05390). This work was supported in part by a grant from the DOE Theoretical Ecology Program (#DE-FG02-90ER60932). We thank Dave Schimel, Ingrid Burke, Dennis Ojima, Kevin Gallo, Tom Vonder Haar and Zeng Xubin for their assistance. We are grateful to Jeff Eidenshink (USGS EROS Data Center) who provided NDVI images. The paper was ably edited and prepared, as usual, by Dallas McDonald.

Material for this paper was extracted from a more extended conference paper entitled "Influence of mesoscale landuse on weather and climate and its representation for use in large scale models" by R.A. Pielke, G.A. Dalu, J.R. Garratt, T.G.F. Kittel, R.A. Stocker, T.J. Lee, and J.S. Snook presented at the Indo-U.S. Seminar on "The Parameterization of Subgrid-Scale Processes in Dynamical Models of Medium-Range Prediction and Global Climate" in Pune, India, August 6-10, 1990.

6. References

- André, J.-C., P. Bougeault, and J.-P. Goutorbe, 1990: Regional estimates of heat and evaporation fluxes over non-homogeneous terrain. Examples from the HAPEX-MOBILHY Programme. *Bound.-Layer Meteor.*, **50**, 77-108.
- Avissar, R. and Y. Mahrer, 1988: Mapping frost-sensitive areas with a three-dimensional local-scale numerical model. Part I: Physical and numerical aspects. *J. Appl. Meteor.*, **27**, 400-413.
- Avissar, R. and R.A. Pielke, 1989: A parameterization of heterogeneous land surfaces for atmospheric numerical models and its impact on regional meteorology. *Mon. Wea. Rev.*, **117**, 2113-2136.
- Barnett, T.L. and D.R. Thompson, 1983: Large-area relation of Landsat MSS and NOAA-6 AVHRR spectral data to wheat yields. *Remote Sens. Environ.*, **13**, 227-290.
- Burke, I.C., C.M. Yonker, W.J. Parton, C.V. Cole, K. Flach, and D.S. Schimel, 1989: Texture, climate, and cultivation effects on soil organic matter content in U.S. grassland soils. *Soil Science Soc. Amer. J.*, **53**, 800-805.
- Burke, I.C., D.S. Schimel, C.M. Yonker, W.J. Parton, L.A. Joyce, and W.K. Lauenroth, 1990: Regional modeling of grassland biogeochemistry using GIS. *Landscape Ecology*, **4**, 45-54.
- Burke, I.C., T.G.F. Kittel, W.K. Lauenroth, P. Snook, and C.M. Yonker, 1991: Regional analysis of the central Great Plains: Sensitivity to climate variability. *Bioscience*, (submitted).
- Dalu, G.A. and R.A. Pielke, 1991: Vertical heat fluxes generated by mesoscale atmospheric flow induced by thermal inhomogeneities in the PBL. *J. Atmos. Sci.*, (submitted).

- Davis, F.W., J. Michaelsen, R. Dubayah, and J. Dozier, 1990: Optimal terrain stratification for integrating ground data from FIFE. In: *Symposium on FIFE*, F.G. Hall and P.J. Sellers (Eds.), February 7-9, 1990, Anaheim, California. American Meteorological Society, Boston, 6-12.
- Davis, F.W., D.S. Schimel, M.A. Friedl, J.C. Michaelson, T.G.F. Kittel, R. Dubayah, and J. Dozier, 1991: Correspondence of surface climate variables and digitized terrain data over a tallgrass prairie. *J. Geophys. Res.*, (submitted).
- Desjardins, R.L., P.H. Schuepp, and J.I. MacPherson, 1990: Spatial and temporal variations of CO₂, sensible and latent heat fluxes over the FIFE site. Pages 46-168 in F.G. Hall and P.J. Sellers, conveners. *Symposium on the First ISLSCP Field Experiment (FIFE)*. American Meteorological Society, Boston, MA.
- Goward, S.N., C.J. Tucker, and D.G. Dye, 1986: North American vegetation patterns observed with the NOAA-7 Advanced Very High Resolution Radiometer. *Vegetatio*, **64**, 3-14.
- Hadfield, M.G., W.R. Cotton, and R.A. Pielke, 1991a: Large-eddy simulations of a small-scale, thermally forced circulation in the convective boundary layer. *Bound.-Layer Meteor.*, (submitted).
- Hadfield, M.G., W.R. Cotton, and R.A. Pielke, 1991b: Thermally forced circulations in the convective boundary layer - the effect of changes in wavelength and wind speed. *Bound.-Layer Meteor.*, (submitted).
- Justice, C.O., J.R.G. Townsend, B.N. Holben, and C.J. Tucker, 1985: Analysis of the phenology of global vegetation using meteorological satellite data. *Int. J. Remote Sens.*, **6**, 1271-1318.
- Kittel, T.G.F., A.K. Knapp, T. Seastedt, and D.S. Schimel, 1990: A landscape view of biomass, LAI, and photosynthetic capacity for FIFE. In: *Symposium on FIFE*, F.G. Hall and P.J. Sellers

- (Eds.), February 7-9, 1990, Anaheim, California. American Meteorological Society, Boston, 66-69.
- Lanicci, J.M., T.N. Carlson, and T.T. Warner, 1987: Sensitivity of the Great Plains severe-storm environment to soil-moisture distribution. *Mon. Wea. Rev.*, **115**, 2660-2673.
- Parton, W.J., D.S. Schimel, C.V. Cole, and D.S. Ojima, 1987: Analysis of factors controlling soil organic matter levels in Great Plains grasslands. *Soil Science Soc. Amer. J.*, **51**, 1173-1179.
- Pielke, R.A. and E. Kennedy, 1980: Mesoscale terrain features, January 1980. Report # UVA-ENV SCI-MESO-1980-1, 29 pp.
- Pielke, R.A. and R. Avissar, 1990: Influence of landscape structure on local and regional climate. *Landscape Ecology*, **4**, 133-155.
- Running, S.R., R.R. Nemani, D.L. Peterson, L.E. Band, D.F. Potts, L.L. Pierce, and M.A. Spanner, 1989: Mapping regional forest evapotranspiration and photosynthesis by coupling satellite data with ecosystem simulation. *Ecology*, **70**, 1090-1101.
- Schimel, D.S., T.G. F. Kittel, A.K. Knapp, T.R. Seastedt, W.J. Parton, and V.B. Brown, 1991: Physiological interactions along resource gradients in a tallgrass prairie. *Ecology*, (in press).
- Schmidt, J.M. and W.R. Cotton, 1990: Interactions between upper and lower tropospheric gravity waves on squall line structure and maintenance. *J. Atmos. Sci.*, **47**, 1205-1222.
- Schols, J.L. and E.W. Eloranta, 1991: Calculation of area-averaged vertical profiles of the horizontal wind velocity from volume-imaging LIDAR data. *J. Geophys. Res.*, (submitted).
- Segal, M., R. Avissar, M.C. McCumber, and R.A. Pielke, 1988: Evaluation of vegetation effects on the generation and modification of mesoscale circulations. *J. Atmos. Sci.*, **45**, 2268-2392.

- Sellers, P.J., 1985: Canopy reflectance, photosynthesis, and transpiration. *Int. J. Remote Sens.*, **6**, 1335-1372.
- Steyn, D.G. and K.W. Ayotte, 1985: Application of two-dimensional terrain height spectra to mesoscale modeling. *J. Atmos. Sci.*, **42**, 2884-2887.
- Tremback, C.J. and R. Kessler, 1985: A surface temperature and moisture parameterization for use in mesoscale numerical models. *7th Conference on Numerical Weather Prediction*, June 17-20, 1985, Montreal, Quebec, Canada.
- Tremback, C., G. Tripoli, R.W. Arritt, W.R. Cotton, and R.A. Pielke, 1986: The regional atmospheric modeling system. *Envirosoft 86 Conference*, November 19-21, 1986, Newport Beach, California. Appears in the Proceedings of the International Conference on Development and Application of Computer Techniques to Environmental Studies, Los Angeles, California, 601-608.
- Tucker, C.J., J.R.G. Townsend, and T.E. Goff, 1985: African land-cover classification using satellite data. *Science*, **227**, 369-375.
- Tucker, C.J., I.Y. Fung, C.D. Keeling, and R.H. Gammon, 1986: Relationship between atmospheric CO₂ variations and a satellite-derived vegetation index. *Nature*, **319**, 195-199.
- Xian, Z. and R.A. Pielke, 1991: The effects of width of land masses on the development of sea breezes. *J. Appl. Meteor.*, (accepted).
- Young, G.S. and R.A. Pielke, 1983: Application of terrain height variance spectra to mesoscale modeling. *J. Atmos. Sci.*, **40**, 2555-2560.

Young, G.S., R.A. Pielke, and R.C. Kessler, 1984: A comparison of the terrain height variance spectra of the front range with that of a hypothetical mountain. *J. Atmos. Sci.*, 41, 1249-1250.

7. List of Figures

Figure 1: NDVI composite image for the period April 27 – May 10, 1990 covering the northern and central U.S. Great Plains. 1 km resolution. Greens are high values and dark browns are low values. (From a map prepared by the EROS Data Center, Sioux Falls, SD.)

Figure 2: NDVI composite images for week periods ending (A) May 10, 1990 and (B) July 27, 1990. Coverage includes most of Kansas (KS), northeastern Oklahoma (OK), and a portion of Missouri (MO). Winter wheat and grain sorghum cropland (W) and Flint Hills rangeland (F) regions are labeled. 1 km resolution. Brightness is scaled equally for both images. Images courtesy of Jeff Eidenshink, EROS Data Center.

Figure 3: Time cross sections of the domain average total vertical heat flux for model levels 2-9 (150 m, 315 m, 497 m, 696 m, 916 m, 1157 m, 1423 m, 1715 m). The surface boundary is (a) homogeneous, (b) 4 km alternating land and water strips, (c) 8 km strips, (d) 16 km strips, (e) 32 km strips, (f) 64 km strips, and (g) 96 km strips. In this and subsequent time cross section figures, the initial time (0) is 0600 LST.

Figure 4: Time cross sections of the domain average subgrid scale vertical heat flux (S) and the domain average explicit vertical heat flux due to mesoscale circulations (M) for model levels 2-4 (150 m, 315 m, 497 m). The surface boundary is (a) 4 km alternating land and water strips, (b) 8 km strips, (c) 16 km strips, (d) 32 km strips, (e) 64 km strips, and (f) 96 km strips.

Figure 5: Time cross sections of the domain average total vertical flux for model levels 2-9 (150 m, 315 m, 497 m, 696 m, 916 m, 1157 m, 1423 m, 1715 m) with an 8 km alternating land and water surface boundary. Model simulations were initialized with a uniform horizontal wind of (a) 5 m s^{-1} , (b) 10 m s^{-1} , and (c) 15 m s^{-1} .

Figure 6: Time cross sections of the domain average subgrid scale vertical heat flux (S) and the domain average explicit vertical heat flux due to mesoscale circulations (M) for model levels 2-4 (150 m, 315 m, 497 m) with an 8 km alternating land and water surface boundary. Model simulations were initialized with a uniform horizontal wind of (a) 5 m s^{-1} , (b) 10 m s^{-1} , and (c) 15 m s^{-1} .

Figure 7: (a) Vertically integrated, 12 h time and domain averaged total vertical heat flux (T), subgrid scale vertical heat flux (S), and mesoscale vertical heat flux (M). 12 h time and domain averaged (b) total vertical heat flux, (c) subgrid scale vertical heat flux, and (d) mesoscale vertical heat flux for the 19 model experiments at model levels 2-9 (150 m, 315 m, 497 m, 696 m, 916 m, 1157 m, 1423 m, 1715 m). Experiment numbers refer to 1) homogeneous, 2) 4 km strips, 3) 8 km strips, 4) 16 km strips, 5) 32 km strips, 6) 64 km strips, 7) 96 km strips, 8) 4 km strips and 5 m s^{-1} wind, 9) 4 km strips and 10 m s^{-1} wind, 10) 4 km strips and 15 m s^{-1} wind, 11) 8 km strips and 5 m s^{-1} wind, 12) 8 km strips and 10 m s^{-1} wind, 13) 8 km strips and 15 m s^{-1} wind, 14) 16 km strips and 5 m s^{-1} wind, 15) 16 km strips and 10 m s^{-1} wind, (16) 16 km strips and 15 m s^{-1} wind, (17) 32 km strips and 5 m s^{-1} wind, 18) 32 km strips and 10 m s^{-1} wind, and 19) 32 km strips and 15 m s^{-1} wind.

Figure 8: Potential temperature field 12 hours into the model run (1800 LST) for a forest-crop boundary simulation. The forest occupies the left hand side of the domain. Contour interval is 1°K .

Figure 9: Same as Figure 8 but for horizontal velocity field. Contour interval is 0.3 m s^{-1} .

Figure 10: Same as Figure 8 but for vertical velocity field. Contour interval is 0.5 cm s^{-1} . Contour labels have been multiplied by 100.

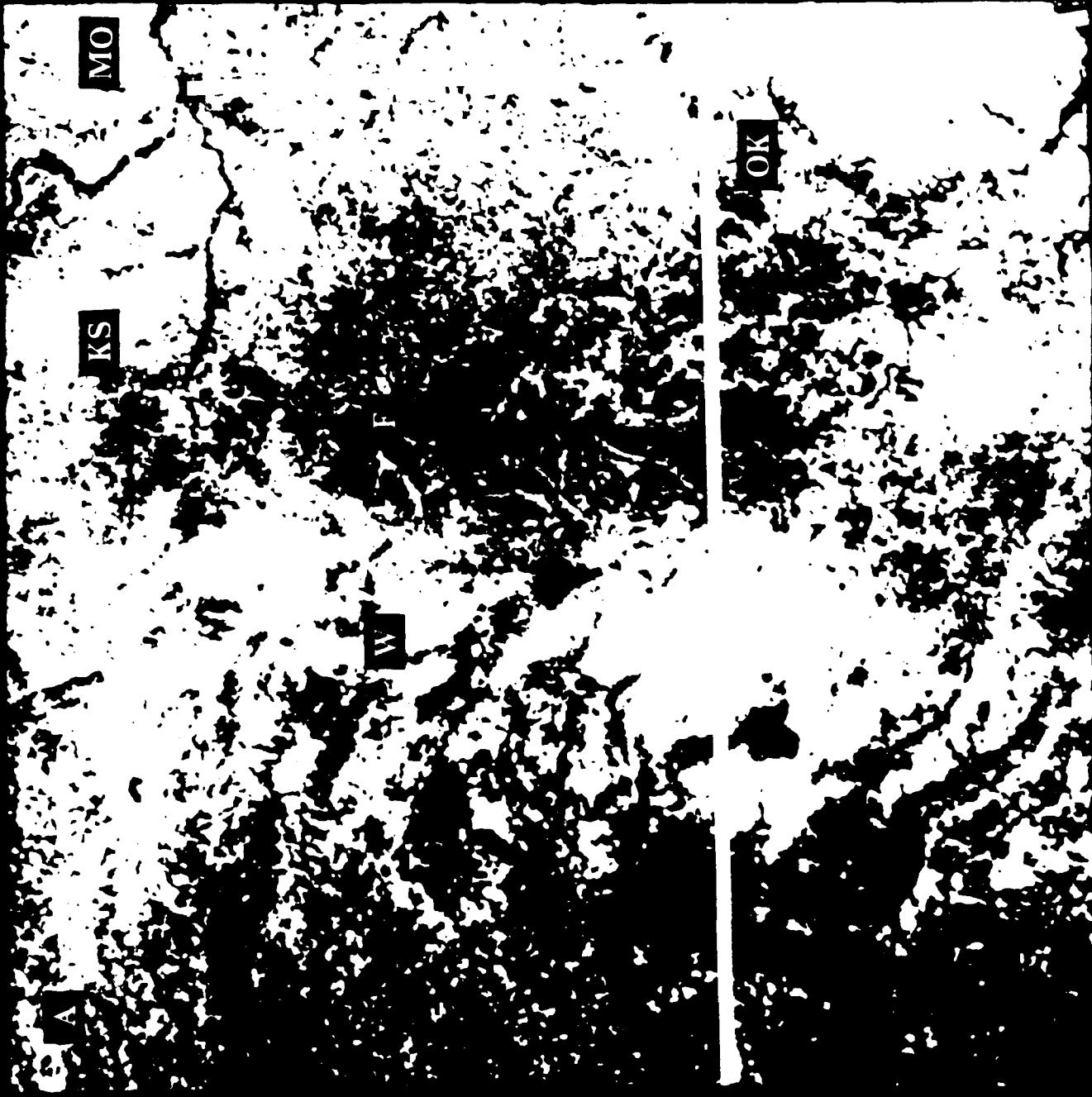
Figure 11: Vertical profile of domain averaged resolvable and subgrid scale heat flux. Subscripts t and c indicate the domain averaged fluxes calculated over the trees and cropland, respectively.

Figure 12: Difference of the resultant heat flux calculated by two different methods. Note that the total difference is the same as the difference in resolvable scale fluxes since the difference in subgrid scale fluxes is zero.



1
+ June 1

← cropping marks



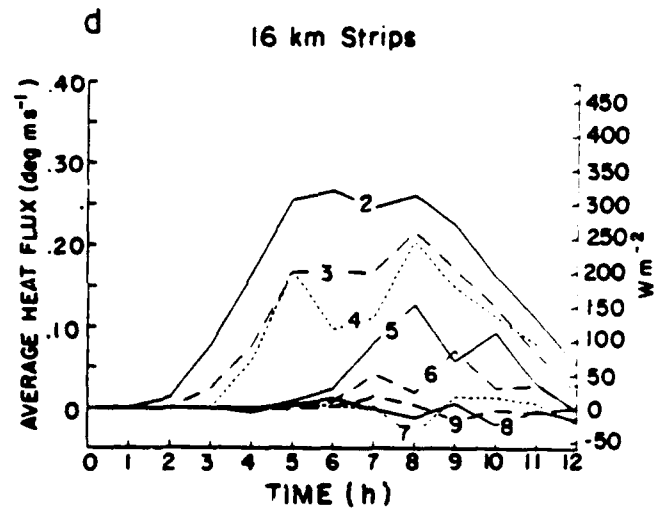
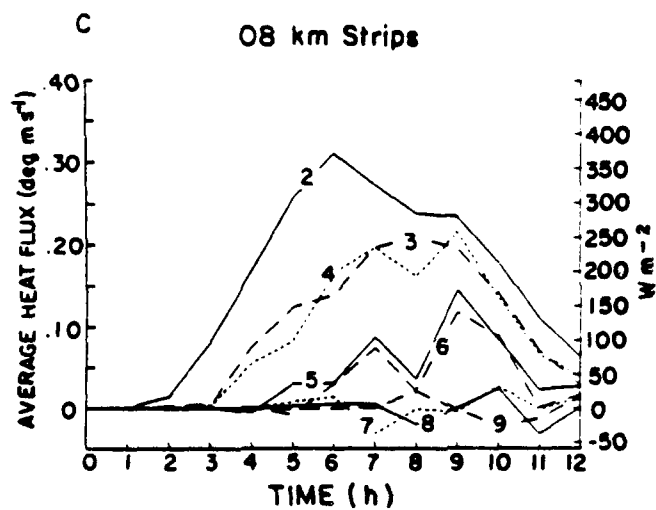
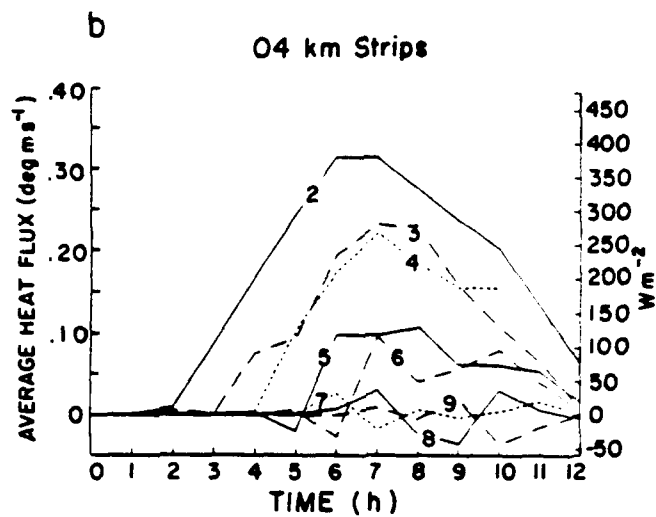
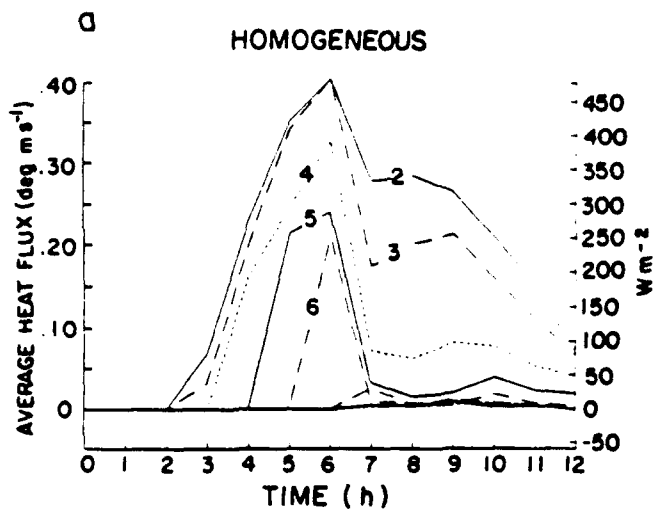
MO

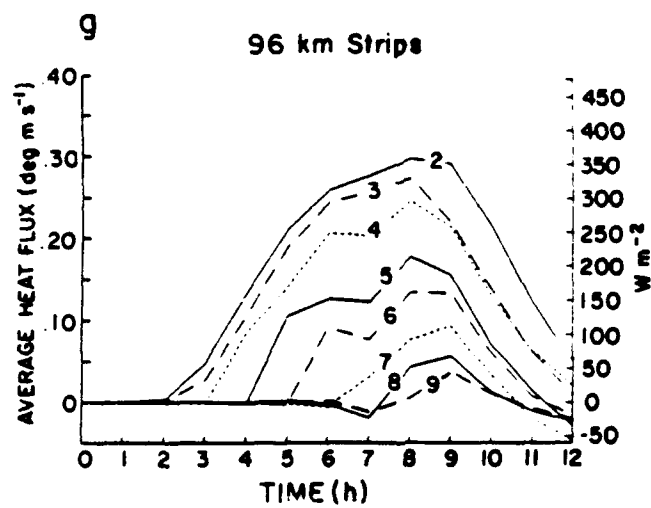
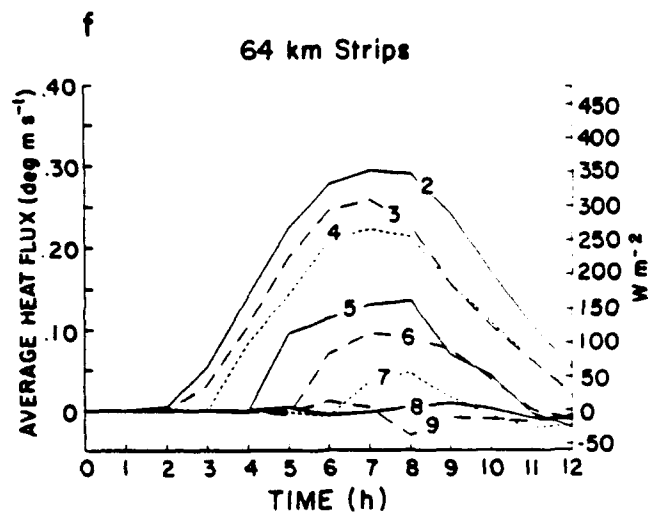
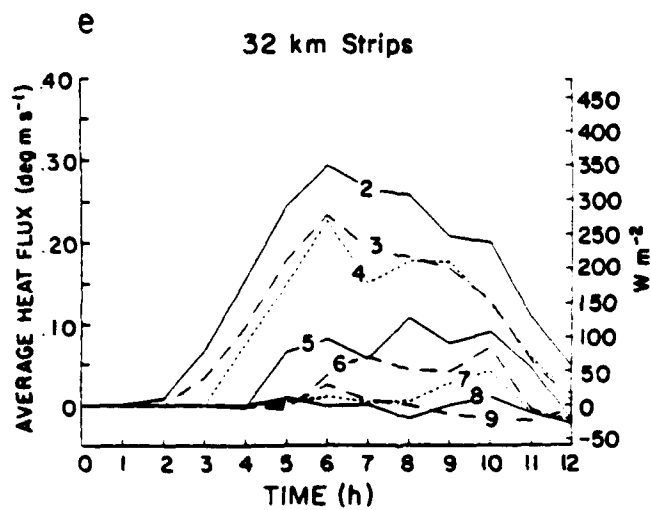
KS

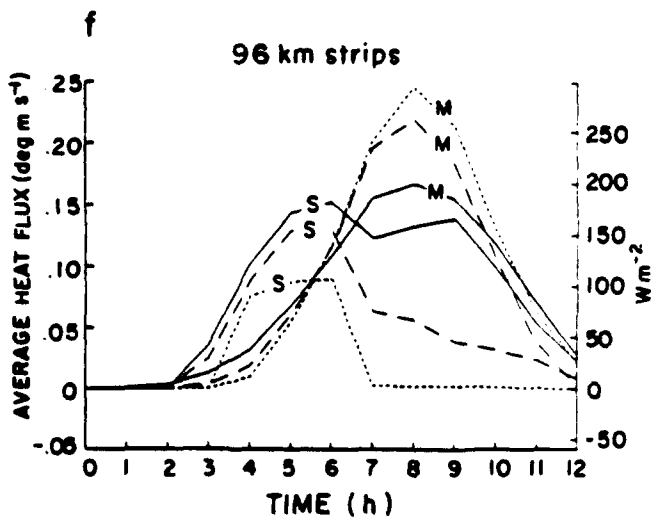
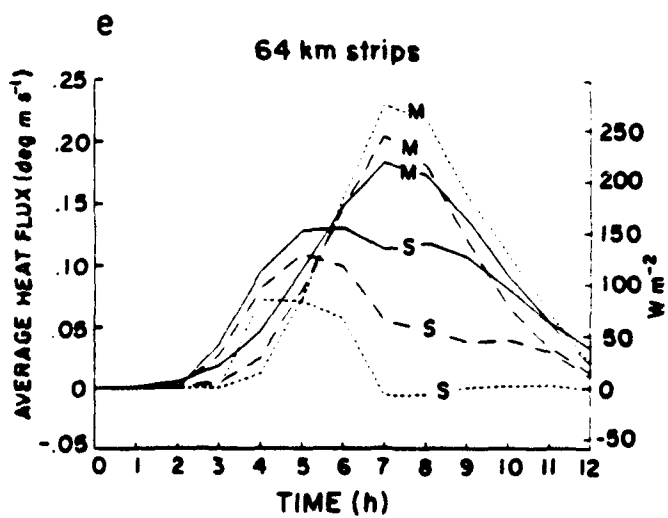
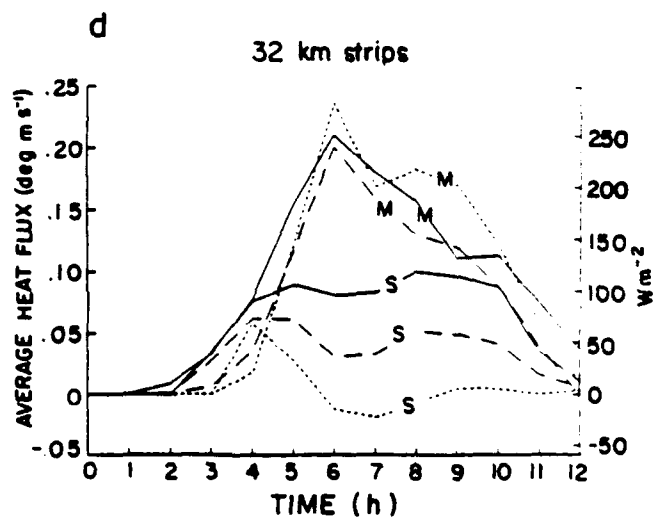
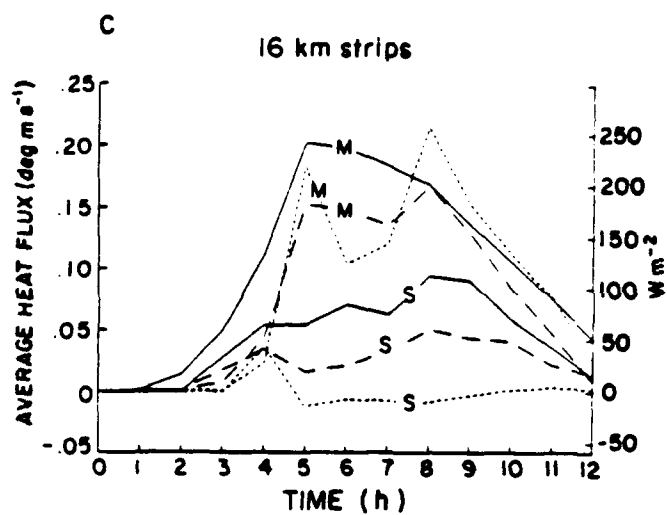
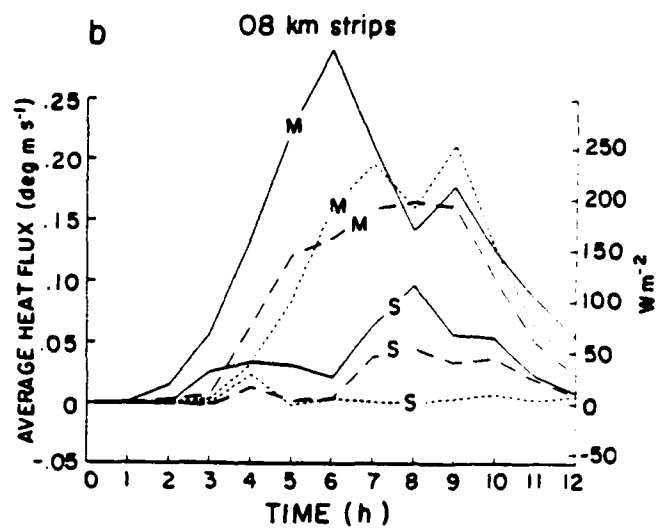
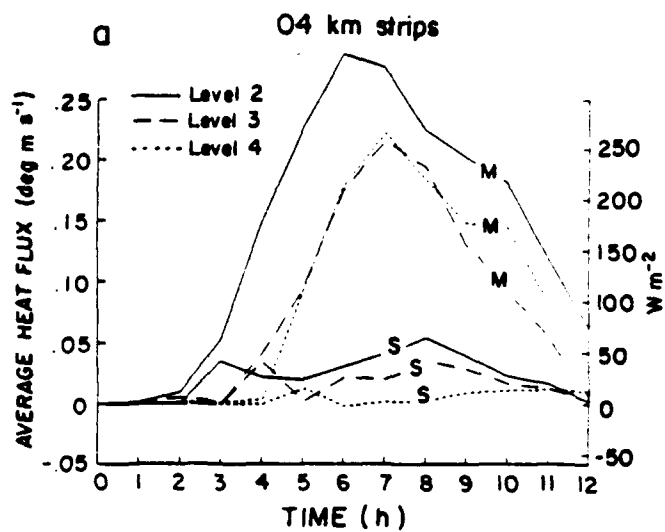
OK

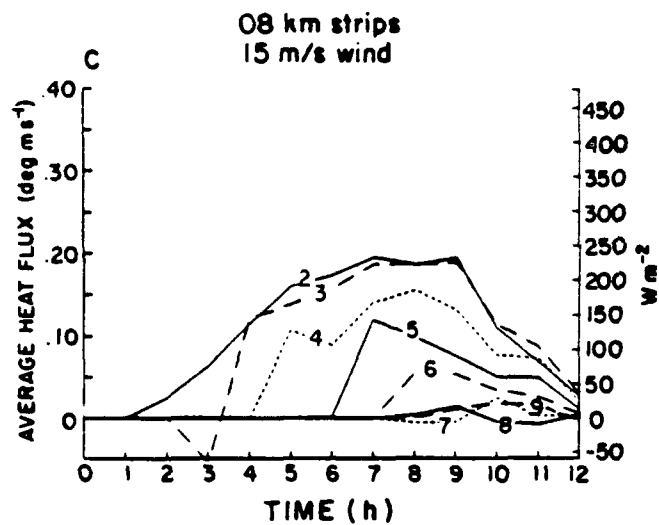
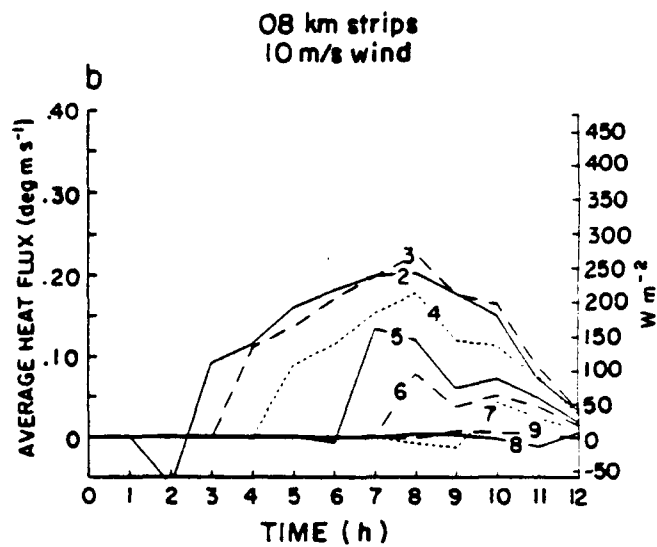
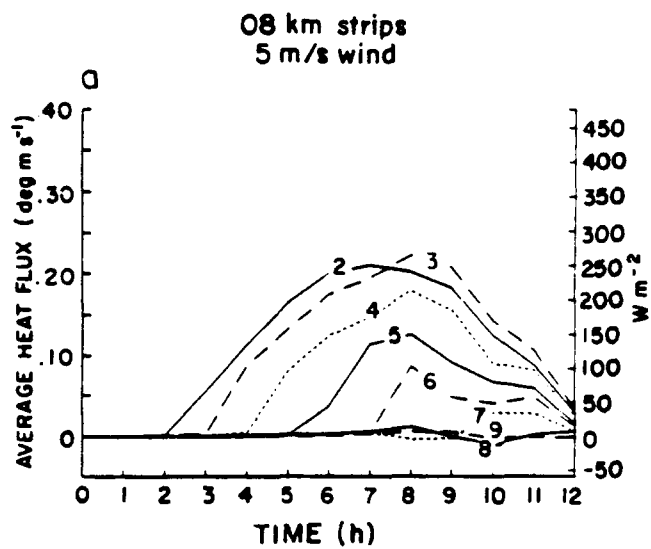
B

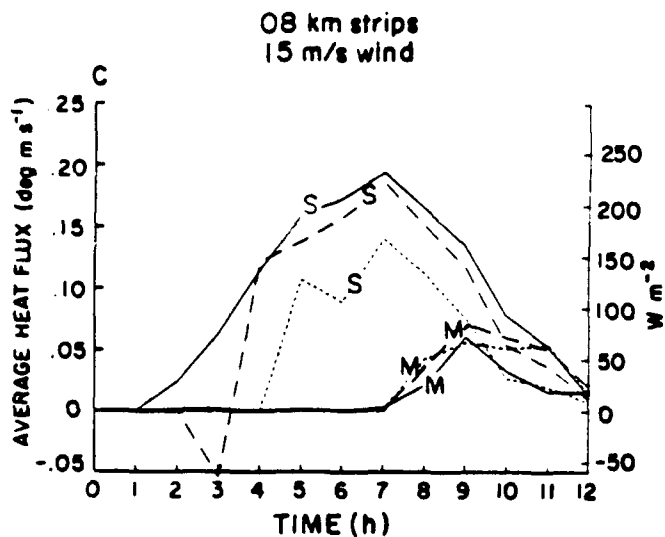
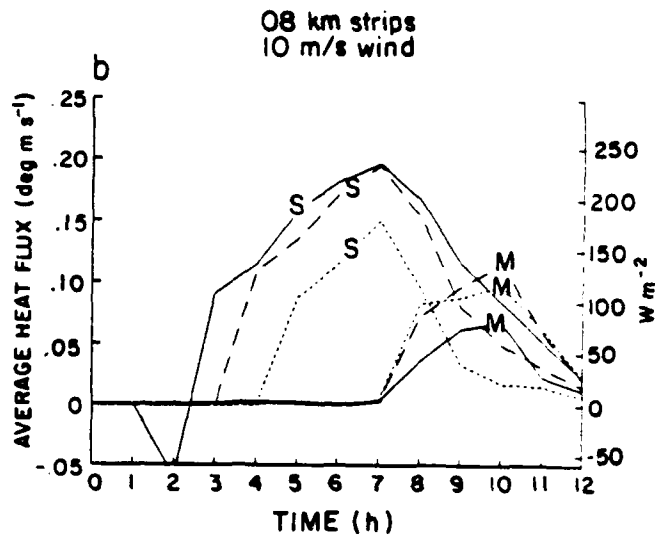
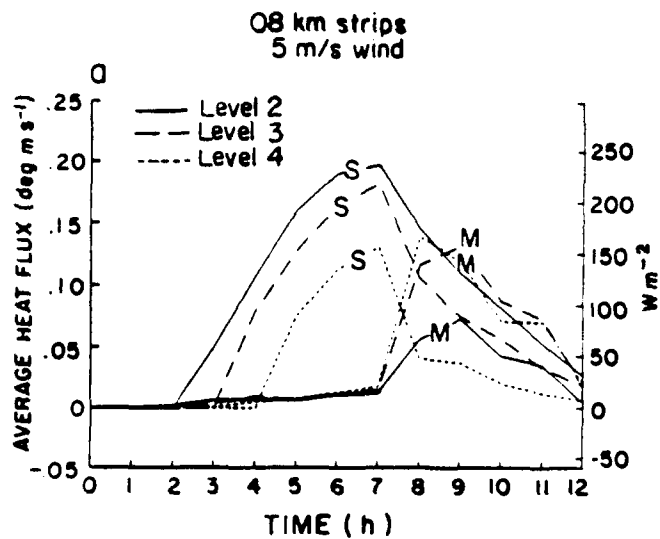
7

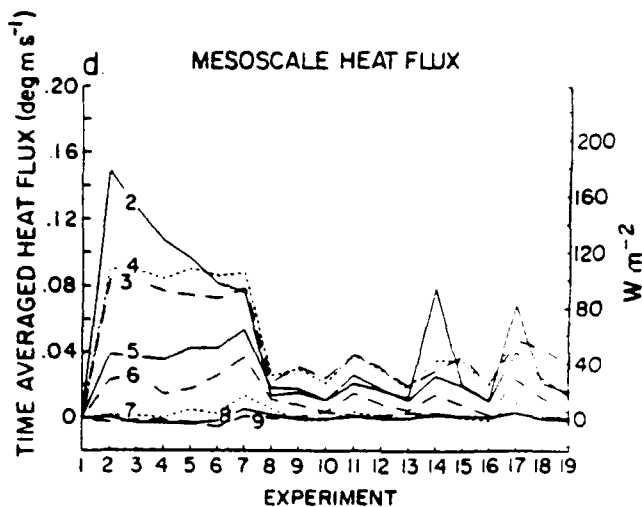
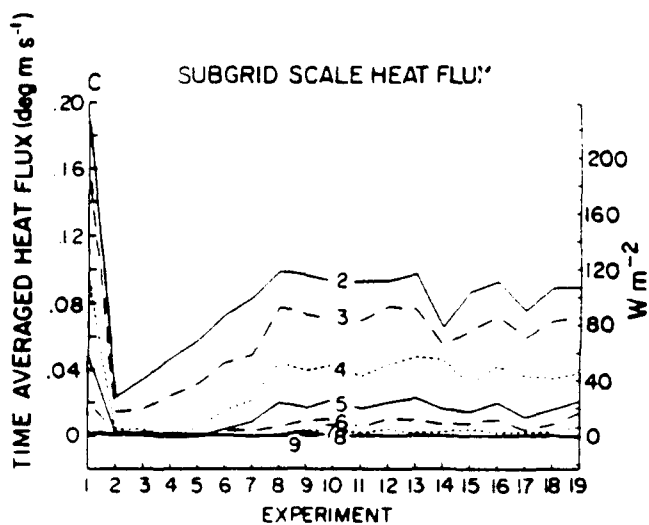
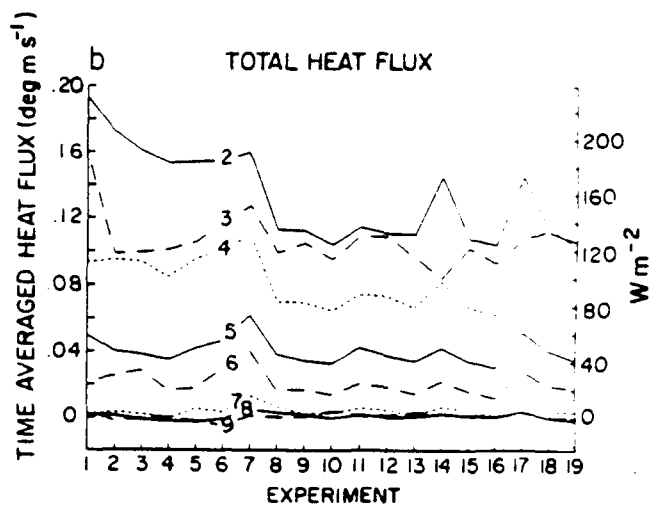
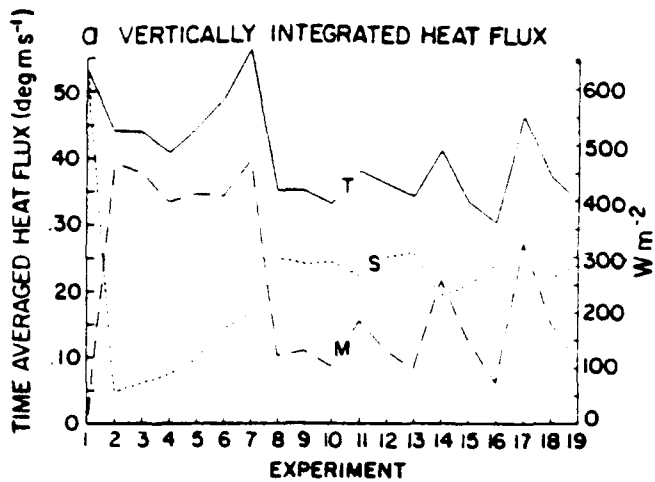












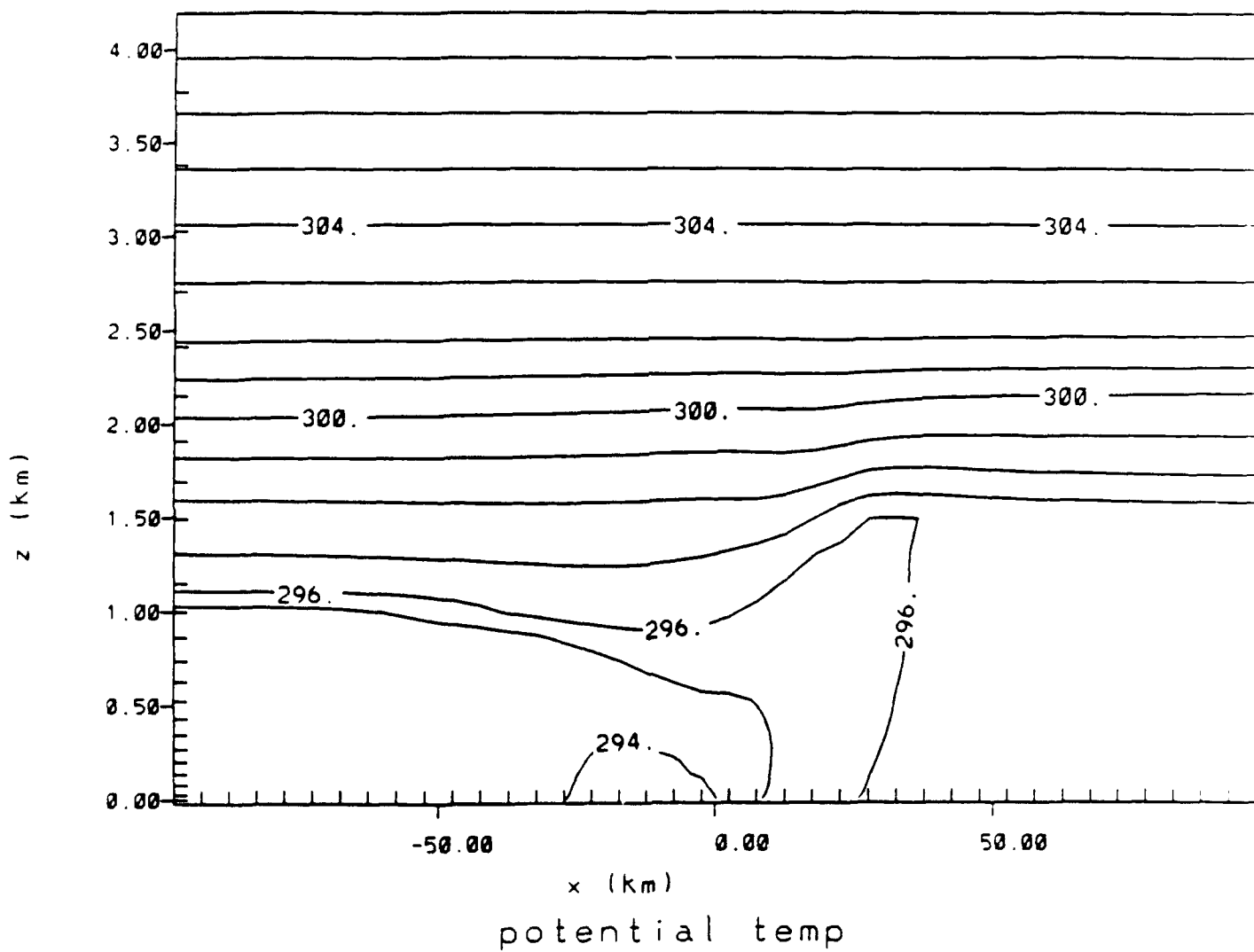


Figure 8

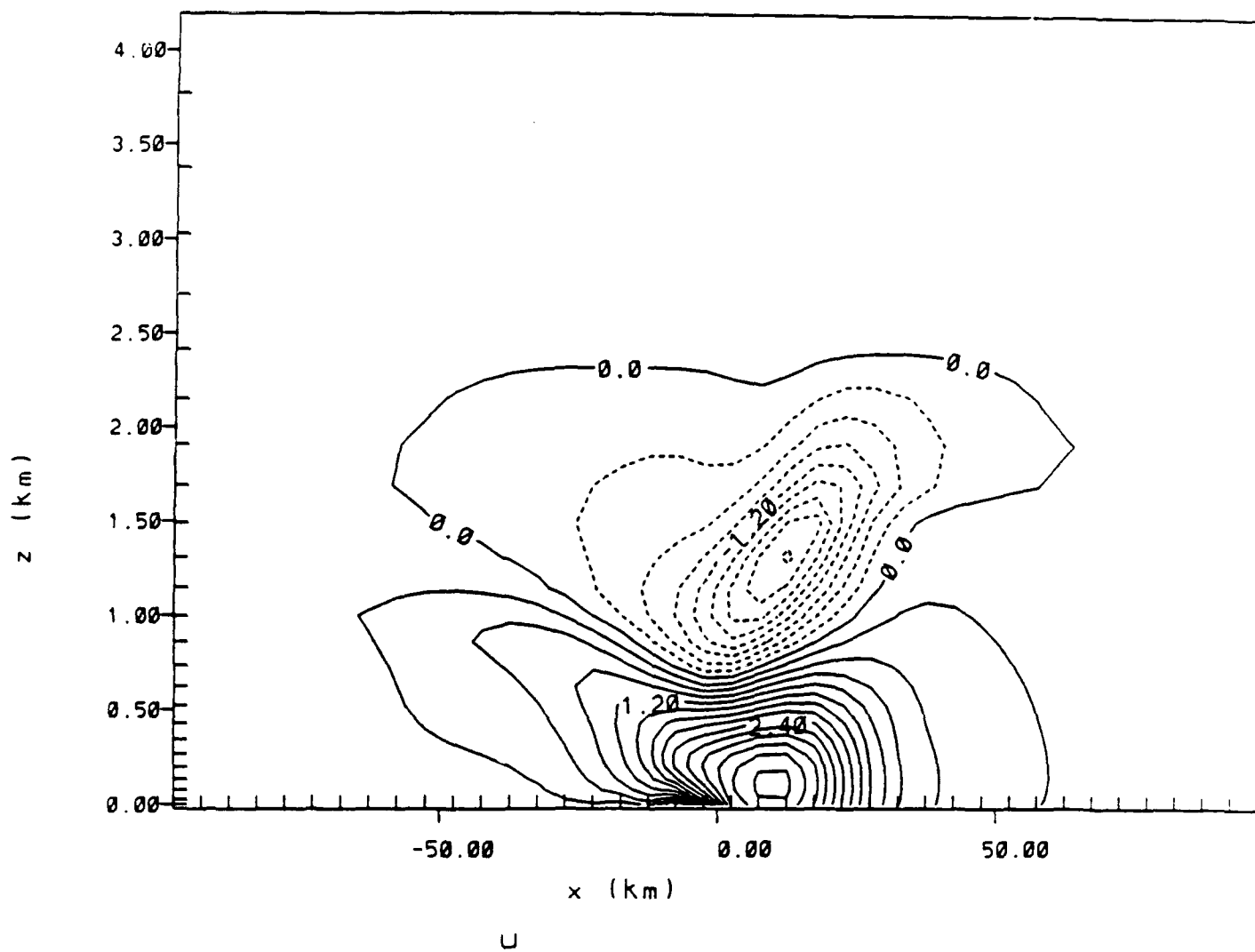
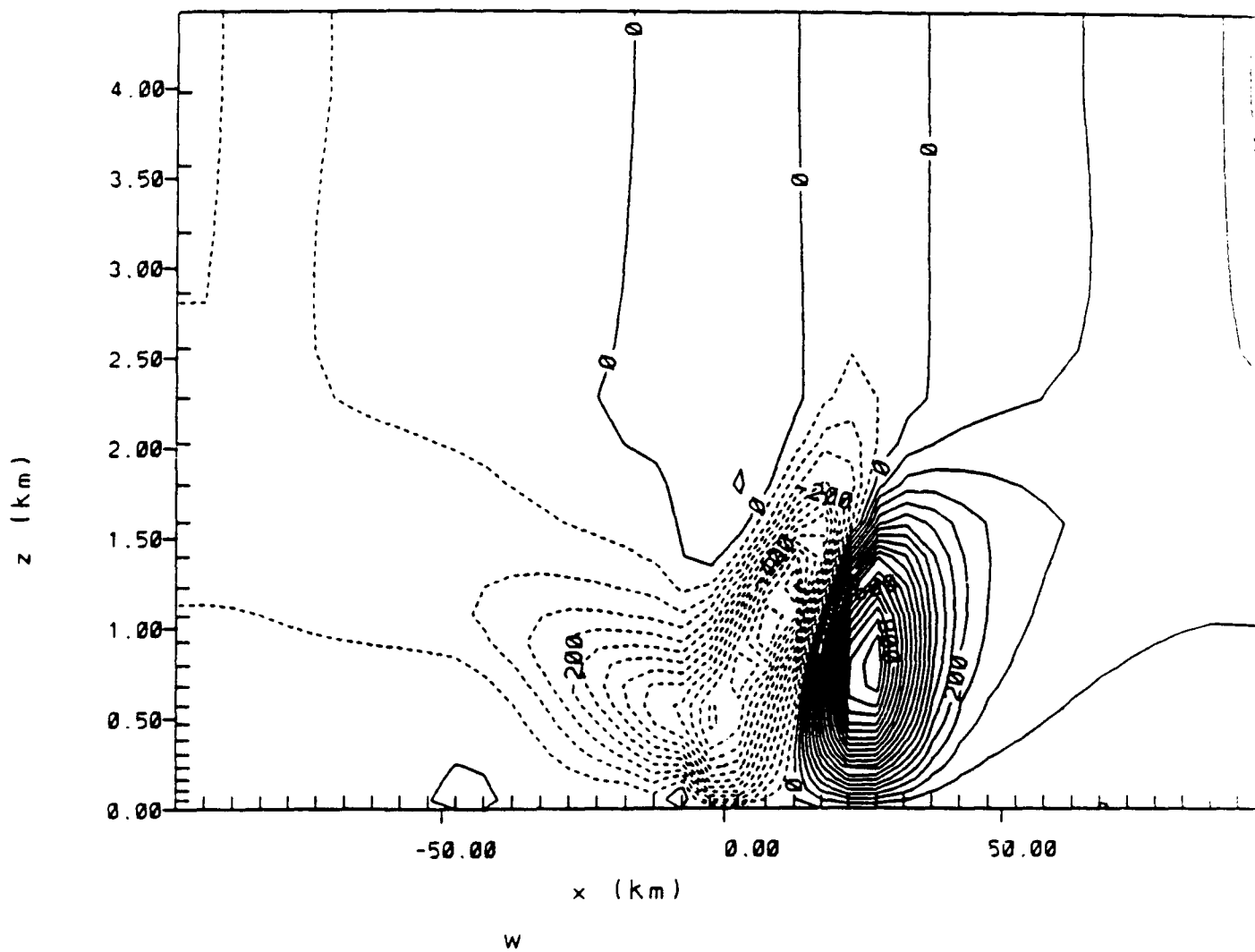


Figure 9



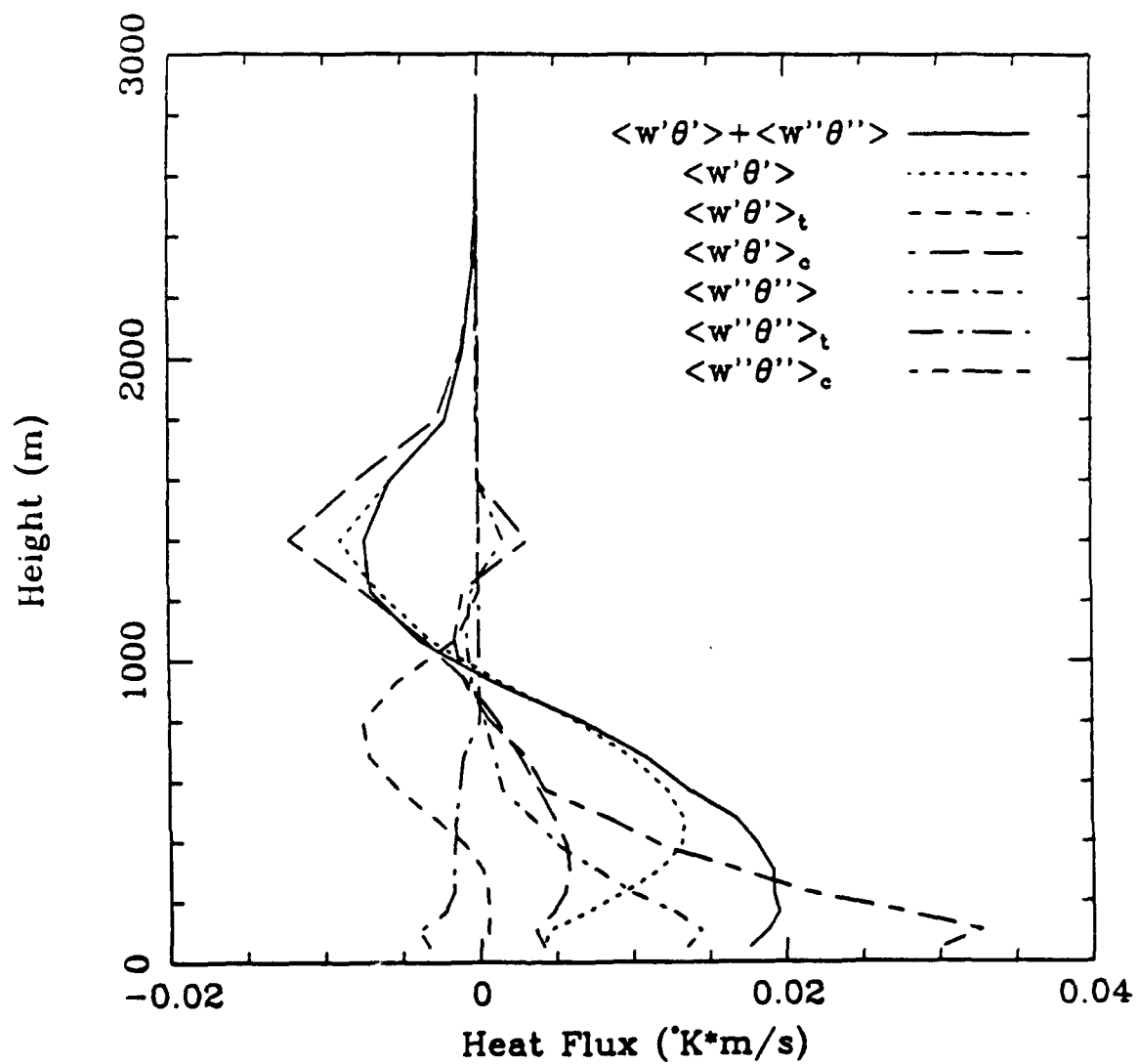


Figure 11

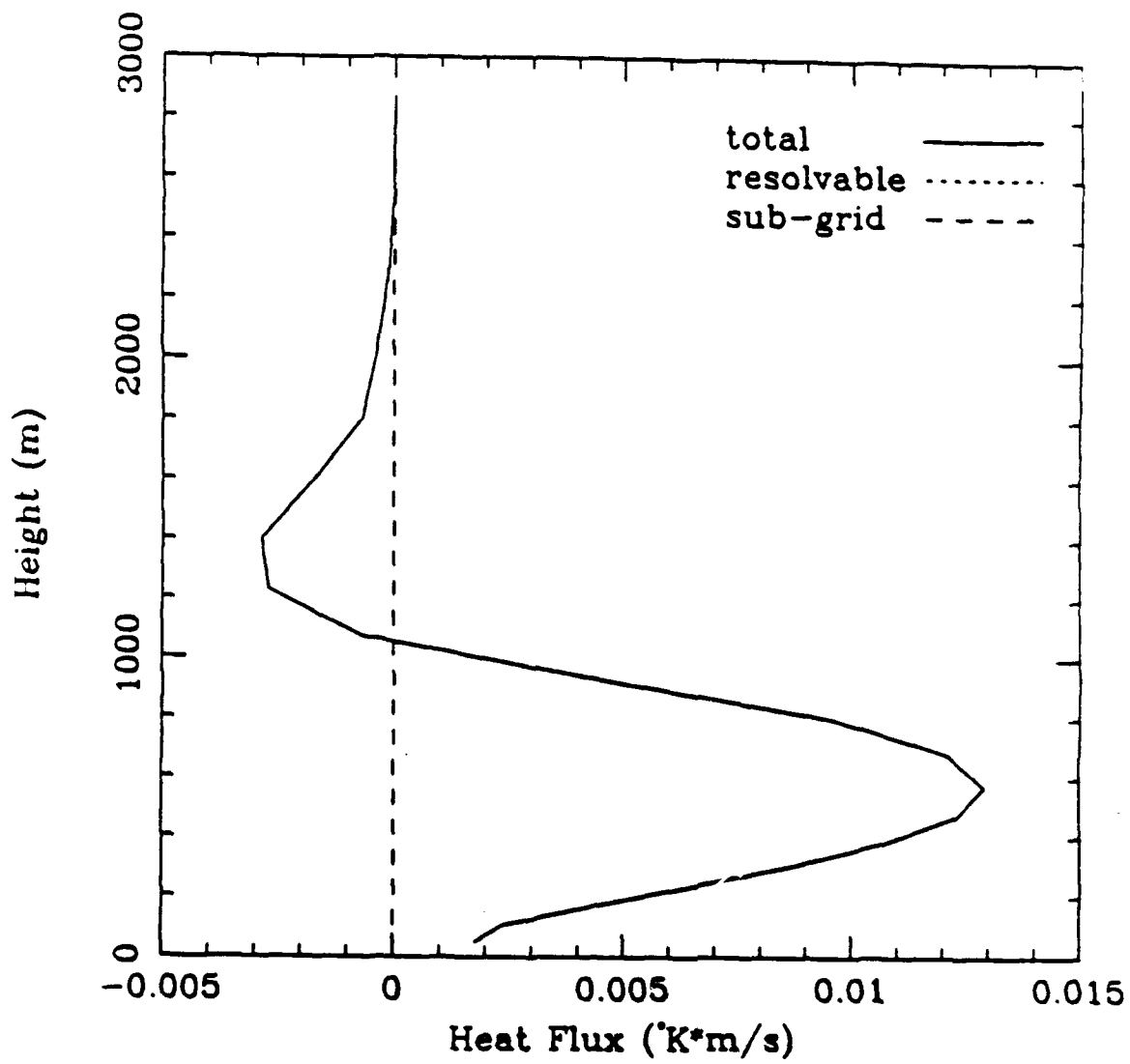


Figure 12